

Wall slip and bulk yielding in soft particle suspensions

Gerhard Jung and Suzanne M. Fielding

Citation: *Journal of Rheology* **65**, 199 (2021); doi: 10.1122/8.0000171

View online: <https://doi.org/10.1122/8.0000171>

View Table of Contents: <https://sor.scitation.org/toc/jor/65/2>

Published by the [The Society of Rheology](#)

ARTICLES YOU MAY BE INTERESTED IN

[Yield stress behavior of colloidal gels with embedded active particles](#)

Journal of Rheology **65**, 225 (2021); <https://doi.org/10.1122/8.0000163>

[Data-driven physics-informed constitutive metamodeling of complex fluids: A multifidelity neural network \(MFNN\) framework](#)

Journal of Rheology **65**, 179 (2021); <https://doi.org/10.1122/8.0000138>

[Transient dynamics of soft particle glasses in startup shear flow. Part I: Microstructure and time scales](#)

Journal of Rheology **65**, 241 (2021); <https://doi.org/10.1122/8.0000165>

[Rheology discussions: The physics of dense suspensions](#)

Journal of Rheology **64**, 1501 (2020); <https://doi.org/10.1122/8.0000174>

[Revisiting the basis of transient rheological material functions: Insights from recoverable strain measurements](#)

Journal of Rheology **65**, 129 (2021); <https://doi.org/10.1122/8.0000154>

[Direct measurements of the microstructural origin of shear-thinning in carbon black suspensions](#)

Journal of Rheology **65**, 145 (2021); <https://doi.org/10.1122/8.0000089>



DISCOVER the **RHEOMETER** with the...
Sensitivity • Ease-of-use • Versatility
to address the most **demanding** applications

The **NEW Discovery Hybrid Rheometer**





Wall slip and bulk yielding in soft particle suspensions

Gerhard Jung^{1,2,3,a)} and Suzanne M. Fielding³

¹*Institut für Theoretische Physik, University of Innsbruck, Technikerstraße 21A, A-6020 Innsbruck, Austria*

²*Institut für Physik, Johannes Gutenberg-Universität Mainz, Staudingerweg 9, 55128 Mainz, Germany*

³*Department of Physics, Durham University, Science Laboratories, South Road, Durham DH1 3LE, United Kingdom*

(Received 14 October 2020; final revision received 16 January 2021; published 12 February 2021)

Abstract

We simulate a dense athermal suspension of soft particles sheared between hard walls of a prescribed roughness profile, fully accounting for the fluid mechanics of the solvent between the particles and for the solid mechanics of changes in the particle shapes. We, thus, capture the widely observed rheological phenomenon of wall slip. For imposed stresses below the material's bulk yield stress, we show the slip to be dominated by a thin solvent layer of high shear at the wall. At higher stresses, it is augmented by an additional contribution from the fluidization of the first few layers of particles near the wall. By systematically varying the wall roughness, we quantify a suppression of slip with increasing roughness. We also elucidate the effects of slip on the dynamics of yielding following the imposition of constant shear stress, characterizing the timescales at which bulk yielding arises and at which slip first sets in. © 2021 The Society of Rheology. <https://doi.org/10.1122/8.0000171>

I. INTRODUCTION

Concentrated suspensions of soft particles, such as microgels [1], emulsions [2], surfactant vesicles [3], block copolymer micelles [4], and multiarm star polymers [5], display both solid and liquid rheological (deformation and flow) properties. Given an imposed shear stress lower than some yield stress, $\sigma < \sigma_y$, they typically show a solidlike creep response in which the shear strain γ slowly increases over time t but with an ever decreasing shear rate, $\dot{\gamma} \sim t^{-\alpha}$. For a larger imposed stress, $\sigma > \sigma_y$, an early-time creep regime is followed after a time that is often fit to the form $\tau_y \propto (\sigma - \sigma_y)^{-\delta}$ [6] by a yielding transition to a fluidized state of steady flow with a time-independent shear rate $\dot{\gamma}$ in which $\sigma(\dot{\gamma})$ is often fit to the “Herschel–Bulkley” form $\sigma = \sigma_y + k\dot{\gamma}^n$ with $n \leq 1$ [7]. During yielding, the shear field within the fluid bulk often becomes highly heterogeneous [6,8].

However, the motion of such materials is determined not only by their bulk properties but also by their interaction with the confining walls. For smooth enough walls, a material will often appear to slip relative to them [9–13]: the velocity profile $v(y)$ across a sheared sample does not meet up with the velocity of the walls but has an apparent mismatch known as the slip velocity, V_s . This has been suggested to arise via a mechanism in which soft particles become deformed by shear and lift away from the wall, leaving a thin lubricating solvent layer across which a strong shear occurs, giving apparent slip [14]. (The hydrodynamic no-slip condition is, however, finally obeyed where the solvent meets the wall.) This is thought to be key to numerous processes in nature and technology, e.g., water-lubricated transport [15], food transport in the gut [16], and the squeezing of red blood cells through capillaries [17].

A series of remarkable experiments have shown wall slip to have a major impact on rheological data, which must be carefully interpreted to disentangle the contributions of the bulk flow and slip [18]. Indeed, the slip radically changes the steady-state flow curve, $\sigma(\dot{\gamma})$, by causing a nonzero apparent flow branch even below the bulk yield stress, $\sigma < \sigma_y$ [14,19]. The steady-state slip velocity $V_s(\sigma)$ typically depends as a power law on σ or $\sigma - \sigma_y$ (below or above σ_y). The value and universality of the exponent remain controversial; depending on the particle packing fraction and wall properties (wetting vs nonwetting), experiments report a quadratic scaling at small stresses [14,19–22] then linear at larger stresses [23] or vice versa [24–28], or a progression from linear to quadratic across an array of suspensions from dilute to jammed [29]. Very recently, a linear scaling was demonstrated at low stresses, universally across many suspensions and wall types, provided contact line effects are removed [27,28], although it is worth noting that the nonlinear scalings of [22,23] were obtained in microchannels without edge effects.

Slip also profoundly influences the *dynamics* of yielding, during which a state of initially solidlike response gives way to a finally fluidized flow [6,8,30–36]. Indeed, yielding often appears to initiate via slip at the wall, before a fluidized band propagates across the bulk to finally fluidize the whole sample. The degree of slip is, however, strongly influenced by confinement [37,38], wall roughness [26,39], or chemical coating [24,40–42], bringing the intriguing prospect of controlling bulk flows by tailoring the wall conditions.

Compared with this remarkable experimental progress, simulation has lagged far behind, despite its potentially central role in addressing experimentally controversial issues such as the scaling of V_s with σ , and the dependence of V_s on features such as wall roughness, which are only rarely varied systematically in experiment [26].

^{a)}Author to whom correspondence should be addressed; electronic mail: gerhard.jung@uibk.ac.at

TABLE I. Parameter values in the molecular dynamics stage.

| Symbol | Parameter | Value |
|-----------------|--|----------------------------|
| P | Number of particles | 400 |
| L_y | Box height | 1.0 [length unit] |
| L_x | Box width | 0.5 |
| ϕ | Area packing fraction | 0.5 |
| M | Particle mass | 1.0 [mass unit] |
| K_{LJ} | LJ energy constant | 1.0 [energy unit] |
| $\sigma_{pp'}$ | LJ length constant (particle-particle) | 1.2 ($R_p + R_{p'}$) |
| $r_{c,pp'}$ | LJ cutoff length (particle-particle) | $\sqrt[6]{2} \sigma_{pp'}$ |
| τ | Langevin time constant | 0.01 |
| T | Temperature | 0.1 |
| Δt | Numerical time step | 5.42×10^{-6} |
| H | Wall separation | 0.44 |
| b | Wall bump radius | [varied] |
| B | Wall bump separation | $5.0b$ |
| $\sigma_{ps'}$ | LJ length constant (particle-wall) | $1.2 R_p$ |
| $r_{c,ps'}$ | LJ cutoff (particle-wall) | $\sqrt[6]{2} \sigma_{ps'}$ |

The contributions of this paper are fourfold. First, we introduce a method of simulating a dense suspension of soft particles sheared between hard walls of any prescribed roughness profile. It fully accounts for the hydrodynamics of the solvent between the particles and near the walls and for the elastic solid mechanics via which the soft particles change shape. It is thus capable of properly capturing rheological wall slip. (Most existing methods instead simply assume a spherical interparticle potential and an effective solvent drag, although more advanced methods also exist [1,43–45].) Second, we quantify the effects of slip on steady-state flow behavior, confirming that it radically changes a material’s flow curve $\sigma(\dot{\gamma})$ by conferring a branch of slip-induced apparent flow even for $\sigma < \sigma_y$. We show that the steady-state slip velocity $V_s = v(\beta)(\sigma - \sigma_y)$ for $\sigma > \sigma_y$, with a transition in which the prefactor v drops sharply above a critical wall roughness β^* , suppressing slip. For $\sigma < \sigma_y$, we separately find $V_s \propto \sigma$ with smooth walls. Below yield, slip is indeed dominated by a thin Newtonian layer at the wall. In important contrast, however, above yield it additionally includes fluidization of the first few layers of particles. Third, we elucidate the effects of slip on the *dynamics* of yielding following the imposition of constant stress, characterizing the timescales $\tau_y(\sigma)$ at which bulk yielding arises and $\tau_s(\sigma, \beta)$ at which the slip first sets in as the material starts to flow. Finally, we show that slip and bulk effects can be disentangled, with master creep and flow curves for the fluid bulk, regardless of wall roughness.

The paper is structured as follows. In Sec. II, we describe our simulation method. Section III details the physical parameters involved and the physical observables measured. In Sec. IV, we present our results, and in Sec. V, we give conclusions and suggestions for future work.

II. SIMULATION METHOD

We now introduce our method for simulating a two-dimensional dense suspension of soft particles, sheared

between hard walls of any prescribed roughness profile. Any reader who is not interested in these technical details can jump directly to Sec. III without loss of thread.

A. Initialization

1. Molecular dynamics of circular particles

We take a box of length L_x and height L_y , with periodic boundaries in x and y . Inside the box, we randomly initialize an ensemble of $p = 1 \dots P$ circular particles in a region of length L_x and height $H - b$ with packing fraction $\phi = 0.5$. (In the next stage, the particles will be expanded to attain a higher ϕ .) To avoid crystallization, we take a bidisperse 50:50 mixture with particle radii in ratio 1:1.4. Particles closer than the distance $r_{c,pp'}$ interact *via* a Lennard–Jones (LJ) potential,

$$\mathbf{F}_p^{\text{LJ}} = -\nabla_p E^{\text{LJ}}(\{\mathbf{X}_{p'}\}), \quad (1)$$

$$E^{\text{LJ}}(\{\mathbf{X}_{p'}\}) = 4K_{\text{LJ}} \sum_{p,p' < p} \left[\left(\frac{\sigma_{pp'}}{X_{pp'}} \right)^{12} - \left(\frac{\sigma_{pp'}}{X_{pp'}} \right)^6 \right]. \quad (2)$$

Here, \mathbf{X}_p is the position of the p th particle, $X_{pp'} = |\mathbf{X}_p - \mathbf{X}_{p'}|$ is the distance between the p and p' th particles, K_{LJ} is a force constant, and $\sigma_{pp'}$ is a length. Each particle also experiences dissipative drag and thermal noise and accordingly obeys (subject to additive corrections from wall interactions to be described as follows) the equation of motion,

$$M\ddot{\mathbf{X}}_p = \mathbf{F}_p^{\text{LJ}} - \frac{M}{\tau} \dot{\mathbf{X}}_p + \mathbf{F}_p^R. \quad (3)$$

Here, M is the particle mass, τ is a time constant, and \mathbf{F}^R is a delta-correlated random variable with zero mean and variance $\frac{k_B T M}{\Delta t \tau}$.

Parallel walls are placed above and below the particle packing a distance $\Delta y = H$ apart. Each comprises a flat line of length L_x , periodically interrupted by semicircular bumps of radius b and separation B , which protrude into the packing. Each wall is discretized into many (N_w) nodes (we shall discuss the value of N_w later in the paper), and each wall node is held in a fixed position. A short-ranged LJ force then additionally acts between the particles and wall nodes. This is of the form of Eq. (2) with the particle labels p' augmented by wall node labels s' . An overview of the parameter values in this molecular dynamics stage is shown in Table I.

To remove particle-particle and particle-wall node overlaps, we first minimize the interaction energy using the Polak–Ribiere version of the conjugate gradient algorithm (provided by the LAMMPS package [46]). The equations of motion, Eq. (3), are then temporally discretized using the Velocity-Verlet algorithm [47] and evolved using LAMMPS [46]¹ with a time step Δt until the ensemble reaches a statistically steady state after a time $\tau_{\text{eq}} = 5000\Delta t$.

¹See <https://lammmps.sandia.gov/>.

2. Particle expansion and shape change

After the molecular dynamics equilibration just described, the boundary of each (initially) circular particle is discretized into evenly distributed surface nodes, separated a distance (initially) of $\Delta s = 2\pi R/N_s$. (We, therefore, use two different values of N_s , in the ratio 1:1.4, to ensure the same Δs for the two particle species.) The particle boundaries are then rendered elastic via a force acting between adjacent nodes around each boundary according to an elastic membrane model [48]. The continuous version of this model is given by

$$\begin{aligned} \mathbf{F}^{\text{elastic}}(s) &= \frac{\partial}{\partial s}(T\boldsymbol{\tau}), \\ \boldsymbol{\tau} &= \frac{\partial \mathbf{X}/\partial s}{|\partial \mathbf{X}/\partial s|}, \\ T &= K_e \left(\frac{\partial \mathbf{X}}{\partial s} - 1 \right), \end{aligned} \quad (4)$$

with boundary tension T , unit tangent $\boldsymbol{\tau}$, and K_e a surface elastic force constant. This force is discretized to calculate the force on each boundary node,

$$\begin{aligned} \mathbf{F}_s^{\text{elastic}} &= \frac{T_{s+1/2}\boldsymbol{\tau}_{s+1/2} - T_{s-1/2}\boldsymbol{\tau}_{s-1/2}}{\Delta s}, \\ \boldsymbol{\tau}_{s+1/2} &= \frac{\mathbf{X}_{s+1} - \mathbf{X}_s}{|\mathbf{X}_{s+1} - \mathbf{X}_s|}, \\ T_{s+1/2} &= K_e \left(\frac{|\mathbf{X}_{s+1} - \mathbf{X}_s|}{\Delta s} - 1 \right). \end{aligned} \quad (5)$$

The index $s = 0 \dots N_s - 1$ runs over the nodes of any particle boundary, with periodic boundary conditions. For clarity, we omit here the particle number label p . Note that the actual distance $|\mathbf{X}_{s+1} - \mathbf{X}_s|$ between any two nodes will change during the simulation, whereas the equilibrium distance remains constant and equal to Δs .

As noted above, parallel walls are located above and below the particle packing a distance $\Delta y = H$ apart. Each wall is discretized into N_w nodes with neighboring nodes separated by the same curvilinear distance Δs that (initially) separates neighboring nodes in the particle boundaries. (Accordingly, the actual number N_w used in any simulation depends on the values of b and B .) The wall nodes remain fixed in position during this part of the simulation. As above, a short-ranged LJ force acts between the nodes of different particles and between particle and wall nodes. This is of the form of Eq. (2) with the particle labels $p'p$ augmented by node labels $s's$.

The particles are expanded by a pressure that acts inside each particle, modeled via a force of amplitude K_p acting on each boundary node along the outward normal,

$$\mathbf{F}_s^{\text{pressure}} = K_p(\boldsymbol{\tau}'_s \times \hat{\mathbf{z}}), \quad (6)$$

with centered tangent $\boldsymbol{\tau}'_s = (\mathbf{X}_{s-1} - \mathbf{X}_{s+1})/|\mathbf{X}_{s-1} - \mathbf{X}_{s+1}|$. The boundary and wall nodes move as $\dot{\mathbf{X}}_s = \mathbf{F}_s/\gamma$, where \mathbf{F}_s is the total force on any node, against a drag γ , without explicit hydrodynamics in this initialization phase. This equation is evolved using the explicit Euler algorithm with a time step Δt . As they expand, the particles change shape due to crowding but avoid overlap via the short-ranged LJ potential. The wall shapes

TABLE II. Parameters values in the particle expansion stage. Values for P , L_x , L_y , H , b , B , [length unit] as in Table I.

| Symbol | Parameter | Value |
|----------------|-------------------------------------|----------------------------|
| N_{s1} | Boundary nodes per smaller particle | 250 |
| K_e | Particle boundary elastic constant | 2.0 [2 × energy unit] |
| K_p | Expansion force constant | 0.5 |
| $\sigma_{ss'}$ | LJ length constant | 0.00125 |
| $r_{c,ss'}$ | LJ cutoff | $\sqrt[3]{2} \sigma_{ss'}$ |
| K_{LJ} | LJ energy constant | 0.01 |
| γ | Drag | 1.0 [sets time unit] |
| Δt | Numerical time step | 1.125×10^{-6} |

remain constant, with particle-wall overlaps also avoided by the LJ potential. The simulation is stopped when the desired area fraction is achieved. An overview of the parameter values in this particle expansion stage is shown in Table II.

B. Shearing with hydrodynamics

The configuration of particle boundary and wall nodes attained at the end of the initialization procedure just described is then transferred to form the initial configuration in a code that now also incorporates shearing and hydrodynamics. In this hydrodynamic code, the Lagrangian particle boundary and wall nodes move relative to a fixed rectangular Eulerian mesh, on which we implement an incompressible Stokes flow. The combined Eulerian and Lagrangian dynamics are handled using an ‘‘immersed boundary method’’ [48]. At any time step, this comprises the following substeps:

1. Given the source forces arising from the current configuration of particle boundary and wall nodes, as mapped onto the Eulerian mesh in step 5 of the previous time step, the Stokes equation is solved to find the fluid velocity on the Eulerian mesh.
2. This Eulerian velocity field is mapped onto the Lagrangian particle boundary and wall nodes.
3. Using these Lagrangian velocities, the Lagrangian positions of the particle boundary nodes are updated. From these new positions, the new Lagrangian forces of the particle boundary nodes are calculated.
4. Again using the Lagrangian velocities from step 2, the Lagrangian positions and forces of the wall boundary nodes are updated.
5. These forces on the Lagrangian particle boundary and wall nodes are mapped to the Eulerian mesh.

Each substep is detailed in the correspondingly numbered subsection that follows.

At the start of the shearing simulation, we set the desired equilibrium distance Δs between adjacent boundary nodes of each particle to be equal to L/N_s , where L is the perimeter of a circle with the same area as that particle. This desired equilibrium distance then remains constant during the shearing simulation that follows. Additionally, the wall nodes are initialized with forces $\mathbf{F}_s = (+\sigma L_x/(N_w \Delta s), 0)$ and $(-\sigma L_x/(N_w \Delta s), 0)$ on the upper and lower walls, respectively, to impose shear stress on the soft particle suspension. The algorithm that follows then keeps this shear stress constant over the course of the simulation (see Table III for parameter values).

TABLE III. Parameters used in the shearing stage. Values for P , L_x , L_y [length unit], H , B , b , N_s , as in Table II and/or I.

| Symbol | Parameter | Value |
|------------------------|-----------------------------------|-------------------------|
| η | Solvent viscosity | 1.0 [viscosity unit] |
| K_e | Particle surface elastic constant | 1.0 [stress unit] |
| ϕ | Particle area fraction | 0.84 |
| R | Average particle radius | 0.0085 |
| σ_{LJ} | LJ length constant | 9dx |
| r_c | LJ cutoff | σ_{LJ} |
| K_{LJ} | LJ energy constant | 10^{-9} |
| N_x, N_y | Number of Eulerian grid points | 4096 L_x , 8192 L_y |
| $\alpha = \Delta s/dx$ | Lagrangian/Eulerian grid ratio | 1.42 |
| K_w | Wall elastic constant | 20 000 |
| Δt | Numerical time step | 0.002 |

1. Stokes flow on the Eulerian mesh

We consider a biperiodic plane of size $L_x \times L_y$ in which are located Lagrangian walls a distance $\Delta y = H$ apart. These will move relative to each other in order to perform shear. In the gap of size H are soft particles and a Newtonian solvent of viscosity η . In the complementary gap of size $L_y - H$, there is Newtonian solvent only. Over the full $L_x \times L_y$ plane, the fluid velocity field $\mathbf{v}(\mathbf{x}, t)$ and pressure field $p(\mathbf{x}, t)$ obey the incompressible Stokes equations,

$$0 = \eta \nabla^2 \mathbf{v} + \mathbf{f} - \nabla p, \quad (7)$$

$$0 = \nabla \cdot \mathbf{v}. \quad (8)$$

Here, $\mathbf{f}(\mathbf{x}, t)$ is a source force density field, which acts only at the walls of the shearing cell and around the boundaries of the soft particles. These Stokes equations are discretized on a fixed rectangular Eulerian mesh of $i = 0 \dots N_x - 1$, $j = 0 \dots N_y - 1$ points, with the same mesh size $dx = L_y/N_y = L_x/N_x$ in both x and y . (We describe below how to map the wall and particle boundary Lagrangian forces onto this Eulerian mesh.) The discretized differential operator is defined as

$$D_x \phi_{ij} = \frac{\phi_{i+1j} - \phi_{i-1j}}{2 dx}, \quad (9)$$

for any discretized field ϕ_{ij} with $D_y \phi_{ij}$ defined similarly. The discretized Stokes equations are then

$$0 = \eta \mathcal{D}^2 \mathbf{u}_{ij} + \mathbf{f}_{ij} - \mathbf{D} p_{ij}, \quad (10)$$

$$0 = \mathbf{D} \cdot \mathbf{u}_{ij}, \quad (11)$$

with $\mathbf{D} = (D_x, D_y, 0)^T$ and $\mathcal{D}^2 = \mathbf{D} \cdot \mathbf{D}$.

We enforce the incompressibility condition by introducing a streamfunction $\Psi(\mathbf{x}, t)$ via $\mathbf{v}_{ij} = \mathbf{D} \times (\Psi_{ij} \hat{\mathbf{z}})$ and eliminate the pressure by taking the curl of Eq. (10),

$$0 = -\eta \mathcal{D}^4 \Psi_{ij} + (\mathbf{D} \times \mathbf{f}_{ij}) \cdot \hat{\mathbf{z}}. \quad (12)$$

This equation can then be solved using fast Fourier transforms (FFTs) with a computational cost that scales as $N_y N_x \ln(N_x N_y)$.

The discrete FT is defined as

$$\hat{\phi}_{k_x, k_y} = \sum_{i=0}^{N_x-1} \sum_{j=0}^{N_y-1} e^{-i(2\pi/N_x)ik_x} e^{-i(2\pi/N_y)jk_y} \phi_{ij}. \quad (13)$$

The FT of Eq. (12) is

$$0 = -\eta \frac{16}{dx^4} \left[\sin^2\left(\frac{\pi k_x}{N_x}\right) + \sin^2\left(\frac{\pi k_y}{N_y}\right) \right]^2 \hat{\Psi}_{k_x, k_y} + \hat{\mathcal{F}}_{k_x, k_y}, \quad (14)$$

where $\hat{\Psi}_{k_x, k_y}$ and $\hat{\mathcal{F}}_{k_x, k_y}$ are FTs of Ψ_{ij} and $(\mathbf{D} \times \mathbf{f}_{ij}) \cdot \hat{\mathbf{z}}$, respectively. For any source force field \mathbf{f}_{ij} , this equation is solved to find the FFT of the streamfunction, $\hat{\Psi}_{k_x, k_y}$. Via the inverse FFT, we find finally the streamfunction Ψ_{ij} and fluid velocity \mathbf{v}_{ij} on the Eulerian mesh.

We define by $\alpha \equiv \Delta s/dx$ the ratio of the parameter Δs , which we recall sets the separation of Lagrangian mesh points and the mesh size dx of the Eulerian grid. The value of this parameter is important to the effectiveness of any immersed boundary simulation. Too large a value will lead to fluid leakage across the particle boundaries [49]. Too small a value leads to an increased computational effort. Throughout we use a value $\alpha = 1.42$.

2. Eulerian to Lagrangian velocity mapping

The discretized velocity field \mathbf{v}_{ij} as calculated on the Eulerian mesh in the previous substep is now interpolated to the Lagrangian particle boundary and wall nodes using the formula

$$\mathbf{V}_s = \sum_{i=0}^{N_x-1} \sum_{j=0}^{N_y-1} \mathbf{v}_{ij} \delta_h(\mathbf{x}_{ij} - \mathbf{X}_s) dx^2. \quad (15)$$

Here, we use a smoothed discretized delta function $\delta_h(\mathbf{x}) = \delta_h(x)\delta_h(y)$ [50] in which

$$\delta_h(x) = \begin{cases} \frac{3}{8} + \frac{\pi}{32} - \frac{x^2}{4}, & \text{for } 0 < \frac{|x|}{dx} \leq 0.5, \\ \frac{1}{4} + \frac{1-|x|}{8} \sqrt{-2+8|x|-4x^2} - \frac{1}{8} \arcsin\left(\sqrt{2}(|x|-1)\right), & \text{for } 0.5 < \frac{|x|}{dx} \leq 1.5, \\ \frac{17}{16} - \frac{\pi}{64} - \frac{3|x|}{4} + \frac{x^2}{8} + \frac{|x|-2}{16} \sqrt{-14+16|x|-4x^2} + \frac{1}{16} \arcsin\left(\sqrt{2}(|x|-2)\right), & \text{for } 1.5 < \frac{|x|}{dx} \leq 2.5, \\ 0, & \text{for } \frac{|x|}{dx} > 2.5. \end{cases} \quad (16)$$

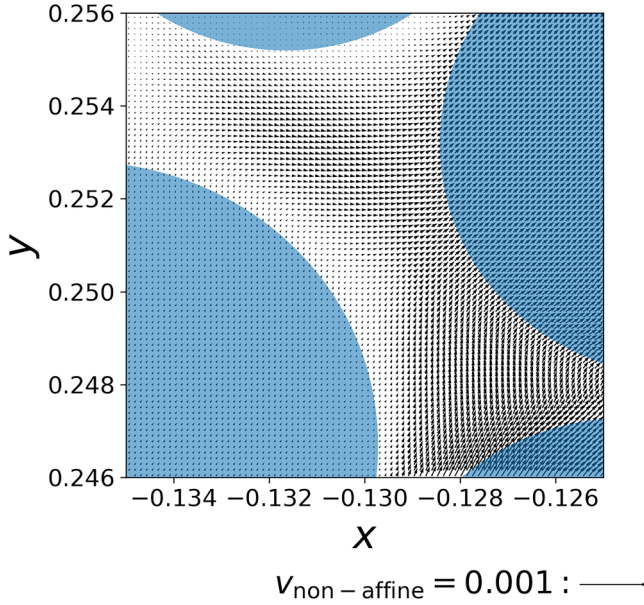


FIG. 1. Simulation snapshot showing the full resolution of the hydrodynamic velocity field. Snapshot taken at time $t = 254.0$ and imposed stress $\sigma = 0.3$. Illustrated are soft particles (blue, see online version for colors) and interparticle fluid (white). Black arrows show nonaffine velocity field v_{na} as defined in Eq. (29).

A snapshot of the soft particles and the velocity field on the Eulerian mesh is shown in Fig. 1. As can be seen, the method is able to fully resolve the hydrodynamic velocity field in the channels, including no-slip boundary conditions and long-range hydrodynamic interactions.

3. Lagrangian dynamics of the particle boundary nodes

Given the Lagrangian velocities of the particle boundary nodes as just calculated, their positions can, in principle, be updated from time step $n \rightarrow n + 1$ simply by using an explicit Euler algorithm,

$$\mathbf{X}_s^{n+1} = \mathbf{X}_s^n + \Delta t \mathbf{V}_s. \quad (17)$$

For clarity, we omit here any particle number label p from \mathbf{X}_s and include only node label s .

With such an update, the area of each particle should, in principle, remain constant due to the incompressibility of the Stokes flow. In practice, however, using the raw \mathbf{V}_s in Eq. (17) gives a small error in particle area conservation due to fluid leakage across the particle boundary. Over the entire simulation, this was about 1% in the worst case. To correct for this, we used the following method [51].

Strict particle area conservation requires that over the area Ω and boundary $\partial\Omega$ of each particle,

$$\int_{\Omega} \nabla \cdot \mathbf{v} \, dA = \int_{\partial\Omega} \mathbf{v} \cdot \mathbf{n} \, dS = 0, \quad (18)$$

where we have used the divergence theorem in writing the first equality. In discretized form, this reads

$$0 = \sum_{s=0}^{N_s-1} \mathbf{V}_s \cdot \hat{\mathbf{n}}_s \Delta S_s, \quad (19)$$

with $\hat{\mathbf{n}}_s = \mathbf{n}_s / |\mathbf{n}_s|$, $\mathbf{n}_s = (Y_{s-1} - Y_{s+1}, X_{s+1} - X_{s-1}, 0)^T$, and $\Delta S_s = |\mathbf{n}_s|/2.0$. To enforce this constraint, we define

$$\mathbf{M} = \sum_{s=0}^{N_s-1} \mathbf{V}_s \cdot \hat{\mathbf{n}}_s \Delta S_s / \sum_{s=0}^{N_s-1} \Delta S_s \quad (20)$$

and subtract this mean value from the normal velocity of any particle boundary node,

$$\mathbf{V}_s \rightarrow \mathbf{V}_s - \mathbf{M} \hat{\mathbf{n}}_s. \quad (21)$$

We use this corrected velocity in the explicit Euler update. With this, the worst case variation in any particle area over a full simulation is smaller than 0.1%.

Given the updated \mathbf{X}_s round the boundary of each particle, the elastic boundary forces $\mathbf{F}_s^{\text{elastic}}$ are then recalculated using Eq. (5). (In this, recall that the value of the equilibrium inter-node length Δs is a constant and equal to its value as at the start of the shearing simulation.)

The nodes of different particles also interact via a weak, truncated LJ force \mathbf{F}_s^{LJ} of the same general form as in Eq. (2). This force introduces a new length scale, σ_{LJ} , which corresponds, for example, to the physics of the van der Waals interaction. The interaction length scale of the LJ potential was empirically adjusted such that the particles never get so close that the finite discretization of the Lagrangian nodes becomes a limitation in the hydrodynamic solver. It, therefore, also ensures that no diverging lubrication forces emerge. Particle nodes also interact with the wall nodes in the same way. The potential used is now of slightly softer form, however, with

$$E^{\text{LJ}}(\{\mathbf{X}_i\}) = 4K_{\text{LJ}} \sum_{s,s' < s} \left(3 \left(\frac{\sigma_{\text{LJ}}}{X_{ss'}} \right)^8 - 4 \left(\frac{\sigma_{\text{LJ}}}{X_{ss'}} \right)^6 \right). \quad (22)$$

The total force on any particle boundary node is then $\mathbf{F}_s = \mathbf{F}_s^{\text{elastic}} + \mathbf{F}_s^{\text{LJ}}$.

4. Lagrangian dynamics of the wall nodes

A schematic of the wall is shown in Fig. 2. The wall itself is modeled as stiff, with the relative distance between wall nodes kept constant using a similar approach as in Eqs. (15) and (16) of [52]. In the following, we describe how to generalize this approach to constant-stress simulations in a channel.

To affect a relative shearing motion of the walls under conditions of a constant imposed shear stress, any node s

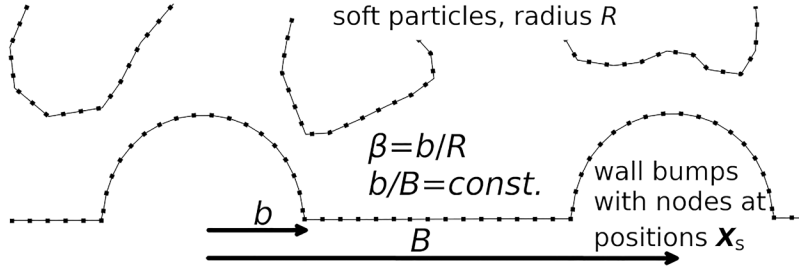


FIG. 2. Schematic of the (lower) wall. The wall is composed of individual nodes at positions X_s^{lower} . The flat parts of the walls are interrupted by regular bumps (semicircles) of radius b separated by a distance B . This sketch is schematic only, for the actual (much larger) resolution of the particle shapes, see Fig. 1.

of the upper wall is tethered at any time t in the simulation via a strong spring force to a desired moving position $X_s^{\text{upper}}(0) + \hat{x} \int_0^t dt \hat{V}^{\text{upper}}(t)$, where $X_s^{\text{upper}}(0)$ is that node's initial location. Accordingly, we have

$$\mathbf{F}_s^{\text{tether,upper}}(t) = -K_w \left[X_s^{\text{upper}}(t) - \left(X_s^{\text{upper}}(0) + \hat{x} \int_0^t dt' \hat{V}^{\text{upper}}(t') \right) \right]. \quad (23)$$

Here, $\hat{V}^{\text{upper}}(t)$ is the time-dependent rightward speed of the upper wall that must obtain (along with a counterpart leftward speed $\hat{V}^{\text{lower}}(t)$ for the lower wall, described below) in order to maintain a constant imposed shear stress in the soft particle suspension between the walls. Our aim in what follows is to calculate these required wall speeds. Averaging Eq. (23) across all nodes in the upper wall, and denoting the average by an overbar, gives

$$L_x \sigma \hat{x} + \frac{L_x}{L_y - H} \eta (\hat{V}^{\text{upper}} + \hat{V}^{\text{lower}}) \hat{x} + G^{\text{upper}} \hat{y} = -K_w \left[\bar{X}_s^{\text{upper}}(t) - \left(\bar{X}_s^{\text{upper}}(0) + \hat{x} \int_0^t dt \hat{V}^{\text{upper}}(t) \right) \right]. \quad (24)$$

The terms on the LHS arise from area-integrating the force balance condition over a rectangle of length L_x that entirely encloses the upper wall. (Recall that force balance states that the divergence of the stress tensor, plus any body forces, must everywhere equal zero.) Converting this area integral to a surface integral via the divergence theorem then gives terms arising from the integral of the shear stress separately along the upper and lower boundaries of that rectangle. The integrals along the sidewalls of the rectangle, G^{upper} , cancel by virtue of the periodic boundary conditions. The upper boundary of the rectangle lies in the solvent outside the walls, with the term in η giving the known shear stress in that Newtonian linear shear profile. (Here, we have assumed that the semicircular wall bumps, which are small on the scale of the channel height $L_y - H$, have a negligible effect on the known result for the shear stress for Newtonian flow between flat parallel walls.) The lower boundary lies in the soft particle packing between the walls. Here, we define σ to be the x -averaged shear stress in that packing, which must be independent of y across the packing.

Taking the time-derivative of the previous two equations gives, respectively,

$$\dot{\mathbf{F}}_s^{\text{tether,upper}}(t) = -K_w [\dot{V}_s^{\text{upper}}(t) - \hat{x} \dot{\hat{V}}^{\text{upper}}(t)] \quad (25)$$

and (writing now only the x component)

$$\frac{L_x \eta (\dot{\hat{V}}^{\text{upper}} + \dot{\hat{V}}^{\text{lower}})}{L_y - H} = -K_w [\bar{V}_x^{\text{upper}}(t) - \dot{\hat{V}}^{\text{upper}}(t)]. \quad (26)$$

Note that the time-derivative of the shear stress σ across the packing, which would appear in Eq. (26), is zero in this constant-stress simulation. Exactly corresponding counterparts to Eqs. (23) to (26) can then be written for the lower wall.

We calculate the Lagrangian velocities V_s of the wall nodes in step 2 above, and thus we can determine their x -components averaged separately across all nodes forming the upper and lower walls, $\bar{V}_x^{\text{upper}}(t)$ and $\bar{V}_x^{\text{lower}}(t)$. Therefore, Eq. (26) and its counterpart for the lower wall form two coupled ordinary differential equations in the desired wall speeds, $\hat{V}^{\text{upper}}(t)$ and $\hat{V}^{\text{lower}}(t)$, that must be imposed to maintain a constant shear stress within the suspension. We update these imposed wall speeds by stepping these ODEs via the explicit Euler algorithm with a time step Δt .

These updated imposed wall speeds $\hat{V}^{\text{upper}}(t)$ and $\hat{V}^{\text{lower}}(t)$, together with the wall node velocities V_s as calculated in step 2, are then substituted into Eq. (25) and its counterpart for the lower wall, which are used to update the tether forces $\mathbf{F}_s^{\text{tether}}$ on the wall nodes, again using the explicit Euler algorithm with a time step Δt .

The velocities V_s of the wall nodes are also used to update the positions of the wall nodes. In principle, we should perform the update using the velocity of each node separately: $X_s^{n+1} = X_s^n + \Delta t V_s$. However, over the course of a simulation, this can lead to a small deformation in the shape of each wall. We, therefore, instead use the average node velocity for each wall. Therefore, for all nodes in the upper wall, we compute

$$X_s^{n+1} = X_s^n + \Delta t \bar{V}^{\text{upper}}, \quad (27)$$

with a corresponding expression for the lower wall.

5. Lagrangian to Eulerian force mapping

The Lagrangian forces on the particle boundary and wall nodes are finally mapped onto the Eulerian mesh. For any particle or either wall, we perform the sum

$$\mathbf{f}_{ij} = \sum_{s=0}^{N_s-1} \mathbf{F}_s \delta_h(\mathbf{x}_{ij} - \mathbf{X}_s) \Delta s \quad (28)$$

(with N_s replaced by N_w for the walls), further summing over all particles and both walls. Here, we use the same discretized delta function as adopted above in Eq. (16) in mapping the Eulerian velocities to the Lagrangian nodes.

III. PHYSICAL PARAMETERS AND OBSERVABLES

The simulation parameters are as follows: the height of the simulation box, $L_y = 1.0$ (length unit); the height of the channel containing the sheared soft particles, $H = 0.44$ (the space of height $L_y - H$ outside the channel contains only Newtonian solvent); the channel length, $L_x = 0.5$; the radius, b , and separation, B , of the wall bumps, which we keep in a fixed ratio $B/b = 5.0$ across all runs; the number of soft particles $N = 800$; the particle boundary elastic constant $K_e = 1.0$ (stress unit); the wall elastic constant $K_{\text{wall}} = 20000.0$; the solvent viscosity $\eta = 1.0$ (viscosity unit); the LJ parameters between nodes of neighboring particles; and the numerical time step and mesh parameters. The particle area fraction is fixed at $\phi = 0.84$ (giving the average particle radius $R = 0.0085$). Combined with the repulsive part of the LJ potential, this ensures that the packing is jammed at rest. Parameters to be explored are then the scaled wall roughness $\beta \equiv b/R$ and imposed shear stress σ .

We measure from our simulations the Lagrangian wall velocities V_{lower} and V_{upper} . The apparent shear rate across the channel is then $\dot{\gamma}_{\text{wall}} = (V_{\text{upper}} - V_{\text{lower}})/H$. This includes a contribution from true shear across the fluid bulk and from a thin slip layer adjacent to each wall. To disentangle these contributions, we measure the flow speed in the main flow direction x at any location on the Eulerian grid between the walls as $v(x, y)$ and average it along x to get the velocity profile $\bar{v}(y)$ across the channel. Over a reduced gap that excludes the slip layers, from $y = y_{\text{lower}} + 5R$ to $y = y_{\text{upper}} - 5R$, we fit $\bar{v}(y)$ to a straight line, $v_{\text{fit}}(y)$. The slope of this line then gives the bulk shear rate $\dot{\gamma}_{\text{bulk}}$, and its wall intercepts give the slip velocities: $V_{s,\text{lower}} = v_{\text{fit}}(y = y_{\text{lower}}) - V_{\text{lower}}$ and $V_{s,\text{upper}} = V_{\text{upper}} - v_{\text{fit}}(y = y_{\text{upper}})$. We report the average slip velocity $V_s = (V_{s,\text{lower}} + V_{s,\text{upper}})/2$. We define the normalized velocity profile $v_{\text{norm}}(y) = (\bar{v}(y) - V_{\text{lower}})/(V_{\text{upper}} - V_{\text{lower}})$ vs $y_{\text{norm}}(y) = (y - y_{\text{lower}})/H$. We have checked that our results for $\dot{\gamma}_{\text{bulk}}$ and V_s show no finite size dependence on H (see the Appendix). $\dot{\gamma}_{\text{wall}}$ of course does depend on H due to the important effect of slip itself. Indeed, this is how slip was measured experimentally [18], before the use of flow velocimetry. We also define the

nonaffine velocity

$$v_{\text{na}}(x, y) = \frac{1}{\dot{\gamma}_{\text{bulk}} H} [v_{\text{Euler}}(x, y) - v_{\text{fit}}(y) \hat{\mathbf{x}}] \quad (29)$$

and characterize the flow heterogeneity in the fluid bulk (over the reduced gap $y_{\text{lower}} + 5R < y' < y_{\text{upper}} - 5R$) as

$$\delta_{\text{het}} = \frac{\sqrt{\Lambda}}{\dot{\gamma}_{\text{bulk}} H \sqrt{N_x N_y}}, \quad (30)$$

with $\Lambda = \sum_{x,y'} [v_{\text{Euler},x}(x, y') - v_{\text{fit}}(y')]^2$.

We also analyze two distinct slip lengths. The Newtonian slip length l_s^{newton} describes the thickness of a channel with purely Newtonian flow directly at the wall. It is defined as the point of the largest curvature in the tangential velocity profile $\bar{v}(y)$ close to the wall, $d^3 \bar{v}(y)/dy^3|_{y=l_s^{\text{newton}}} = 0$. The total slip length l_s^{tot} describes the distance of the wall to an extrapolated point in space for which the tangential velocity component vanishes (corresponding to the typical definition of slip length). This characterizes the full slip layer, which includes the Newtonian layer just described as well as the first few layers of particles near the wall, which experience an increase in fluidization.

Any steady-state quantity reported in this work is averaged in each run between the time t_{ss} at which it visibly attains a steady state and $t_{\text{ss}} + \Delta t$, where $\Delta t \geq 500.0$. Each is further averaged over at least two independent simulations. The error bars then correspond to the standard error in the distribution of the time-series averages across these independent simulations.

A sample particle packing, including the rough boundary, is shown in Fig. 3 to give the reader a visualization of the system. The packing corresponds to a single frame of a movie shown in [56].

IV. RESULTS

A. Steady-state velocity profiles and flow curves

The steady-state normalized profiles [Fig. 4, (left)] reveal two separate contributions to the slip: one from a very thin solvent layer within about $\Delta y = 0.0025$ of the wall (inset) and the other over about $\Delta y = 0.1$, corresponding to an increase in fluidity over the first few particle layers near the wall [26,45,53]. Importantly, we find the first contribution to dominate the total slip at stresses below yield, whereas above yield both are important. We report the total slip because it is more likely to be the one seen in experimental velocimetry of realistic pixel resolution. We note that $\bar{v}(y_{\text{lower}}) = V_{\text{lower}}$ (as seen in the inset) and $\bar{v}(y_{\text{upper}}) = V_{\text{upper}}$, consistent with hydrodynamic no slip for the solvent.

Figure 5 shows the steady-state flow curve relationship between the imposed shear stress σ and the shear rate $\dot{\gamma}$, for several different values of the wall roughness parameter β . (Although in our simulations σ is imposed and $\dot{\gamma}$ measured, we show $\sigma(\dot{\gamma})$ because this is the usual flow-curve representation.) The left panel has as its abscissa the

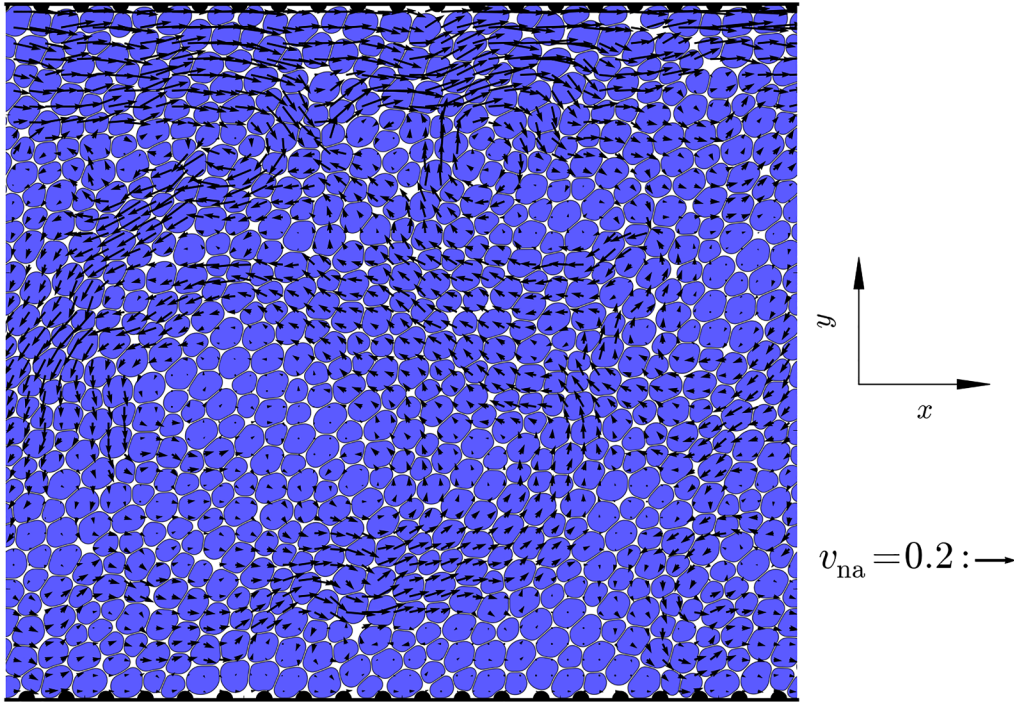


FIG. 3. Simulation snapshot at time $t = 17.5$, as the sample yields. Illustrated are soft particles (blue, see online version for colors), interparticle fluid (white), and rough hard walls (black). Arrows show nonaffine velocity field v_{na} . Wall roughness $\beta = 0.59$ and imposed stress $\sigma = 0.5$.

apparent shear rate, $\dot{\gamma}_{wall}$, defined via the relative wall speed. As noted above, this includes not only any true shear across the fluid bulk but also the effects of wall slip. The right panel uses the true bulk shear rate, $\sigma(\dot{\gamma}_{bulk})$, with slip removed. Above a yield stress, $\sigma > \sigma_y$, the steady-state data superpose for all levels of wall roughness, once the slip is removed. The resulting flow curve is then fit to the Herschel–Bulkley form, $\sigma = \sigma_y + k\dot{\gamma}^n$, with $\sigma_y = 0.055 \pm 0.004$ and $n = 0.57 \pm 0.03$. For lower stresses, $\sigma < \sigma_y$, $\dot{\gamma}_{bulk}$ does not attain a steady state, as indicated by the open symbols in Fig. 5.

B. Heterogeneous flow profiles: Wall slip and bulk yielding

We now further explore the extent to which the flow profiles across the gap are heterogeneous due to wall slip and nonaffine flows in the bulk. Figure 6(a) shows the steady state wall slip velocity as a function of imposed shear stress, for several levels of wall roughness, β . The data for $\sigma > \sigma_y$ are fit for each roughness to the form $V_s = \nu(\beta)(\sigma - \sigma_y)^p$, with $p = 1$. We also find $p = 1$ with an essentially unchanged $\nu(\beta)$ if we instead allow a free intercept, σ'_y . This linear dependence for

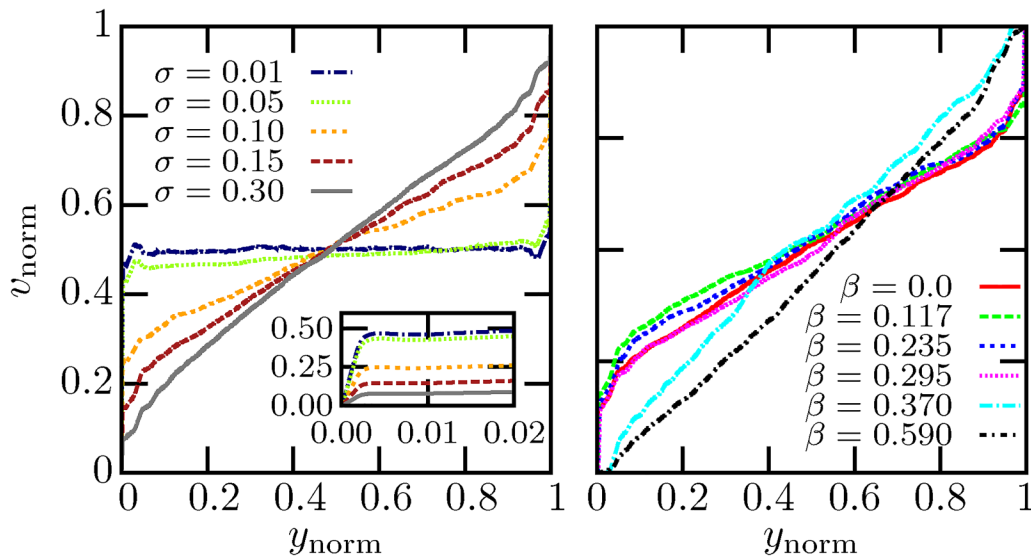


FIG. 4. Steady-state velocity profiles. Left: at several shear stresses for smooth walls, $\beta = 0.0$. Inset: zoom near the wall. Right: several wall roughnesses at shear stress $\sigma = 0.15$.

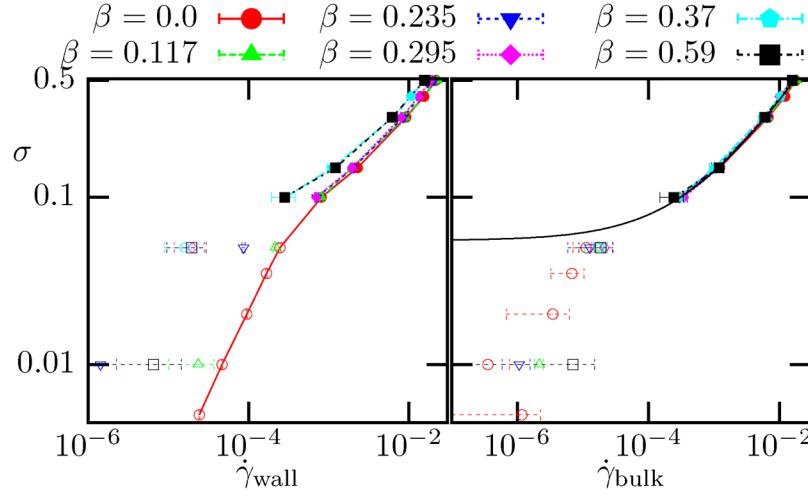


FIG. 5. Left: Apparent flow curves with shear rates calculated from relative wall speeds, including wall slip, for different wall roughnesses β . The solid line connects data points for smooth wall case. Right: Corresponding bulk flow curves using shear rate obtained from internal velocity profile with slip removed. Filled symbols: steady state (errors bars too small to be seen at high stresses). Unfilled symbols: do not attain a steady state, with dashed error bars showing drift during the time $t > 2000$ over which data are taken. Solid line: fit to $\sigma = \sigma_y + k\dot{\gamma}_{\text{bulk}}^n$ with $\sigma_y = 0.055 \pm 0.004$ and $n = 0.57 \pm 0.03$.

$\sigma > \sigma_y$ is consistent with the experiments of [24] and [26], whereas those of [21] and [22] found a quadratic dependence, $p = 2$. In [29], it was suggested that p varies between 1 and 2 as a function of packing fraction ϕ above jamming. It would be interesting in future to simulate a range of ϕ . The prefactor ν , plotted as a function of β in panel c, reveals a transition from strong slip for smooth walls, with $\beta < \beta^* \approx 0.3$, to suppressed slip for rougher walls, $\beta > \beta^*$. A decreasing slip with increasing wall roughness was seen for wall roughnesses less than the average particle size ($\beta < 1$) in [26].

For $\sigma < \sigma_y$, we find a different scaling of the slip velocity, $V_s \propto \sigma$, for smooth walls. (For rough walls, V_s takes prohibitively long to attain a steady state.) That we observe different

scalings for $V_s(\sigma)$ above and below yield is consistent with the discussion above regarding Fig. 4, left: that slip below yield is dominated by a thin solvent layer at the wall, with an additional contribution above yield from fluidization of the first few particle layers.

The transition between the two scalings, below and above yielding, appears to be rather sharp, but a smoother transition is possible within the error bars, which would allow for a small window in which the exponent $p > 1$.

The wall slip can be further characterized using the Newtonian slip length, l_s^{newton} , and the total slip length l_s^{tot} as defined in Sec. III. We observe that the Newtonian slip length is approximately independent of the applied stress σ [see Fig. 7(a)]. The length scale corresponds to the range

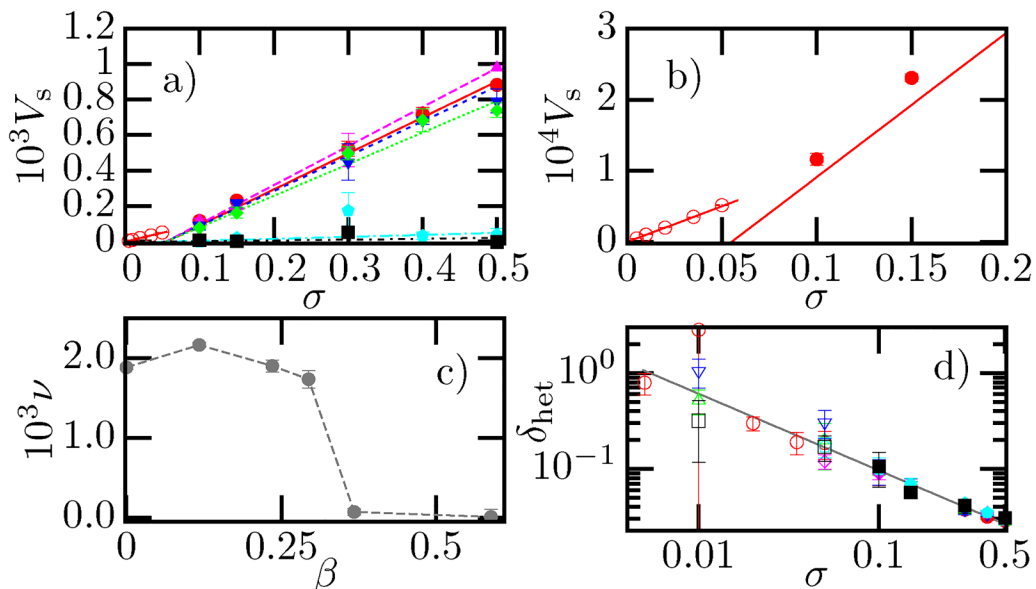


FIG. 6. (a) Symbols: steady-state slip velocity vs imposed stress for different wall roughnesses, with roughness symbol legend as in Fig. 5. Lines: least-square fits to $V_s(\sigma > \sigma_y) = \nu(\beta)(\sigma - \sigma_y)$ and $V_s(\sigma < \sigma_y) = \nu_N(\beta)\sigma$. (b) Zoom of $\beta = 0.0$ data for $\sigma < 0.2$. (c) Prefactor ν vs wall roughness β . (d) Steady-state degree of heterogeneity in the bulk flow field vs imposed stress for different surface roughnesses. Solid line: $\delta_{\text{het}} \propto \sigma^{-0.8}$ as a guide to the eye.

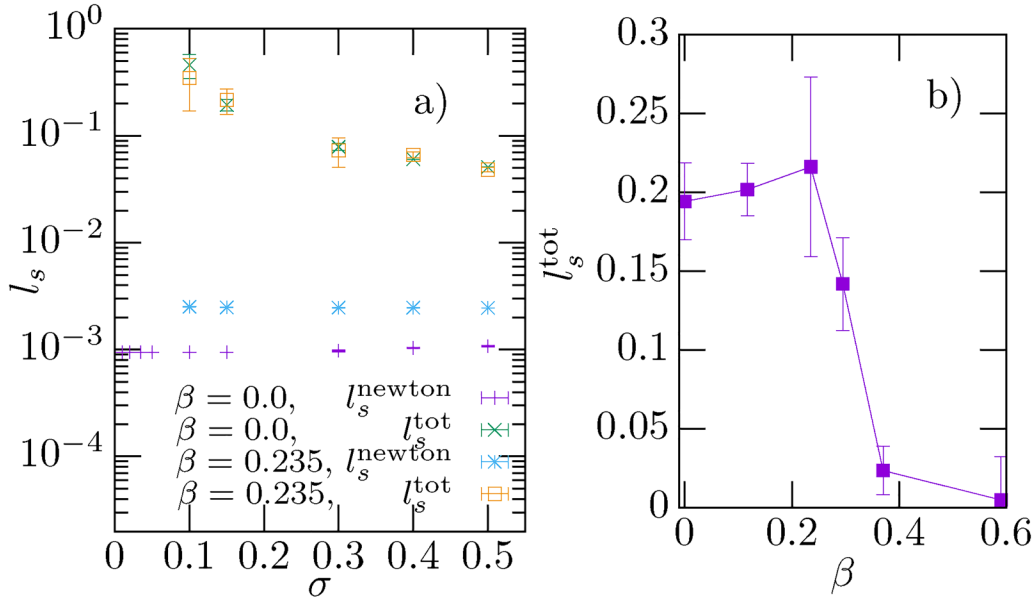


FIG. 7. Steady-state slip length l_s for different external stresses σ (a) and wall roughness β (b). The Newtonian slip length l_s^{newton} describes the thickness of the thin Newtonian layer at the wall and the total slip length l_s^{tot} describes the distance of the wall to an extrapolated point in space for which the tangential velocity component vanishes.

of the LJ interaction between the particles, σ_{LJ} , plus the bump size $b = \beta R$. This indicates that, first, the precise nature of the direct particle-particle and particle-wall significantly influences slip and, second, that below the “critical” roughness $\beta < 0.35$, despite a bump size significantly larger than the particle-wall interactions, a Newtonian slip layer emerges. For $\sigma > 0.2$ and $\beta = 0$ (corresponding to a flat wall), we additionally observe that the particles lift further from the wall than for small stresses (roughly 20% for $\sigma = 0.5$), which could be connected to the process of hydrodynamic lift described in [19]. Contrary to the Newtonian slip length, the total slip length l_s^{tot} does not depend on surface roughness (below $\beta < 0.35$), instead it strongly depends on the applied stress σ . This can be rationalized by the difference in the scaling of the slip velocity V_s (linear) and the true shear rate $\dot{\gamma}_{\text{bulk}}$ (super-linear). Additionally, the total slip length l_s^{tot} displays the same discontinuous transition from slip to no slip that was discussed for V_s [see Fig. 7(b)].

In addition to this apparent slip at the walls, the flow profile within the fluid bulk also shows strong departures from affine shear. This is already apparent in the snapshot of Fig. 3, in which the arrows show the degree to which the flow velocity at any location differs from a simple linear shear profile. In Fig. 6(d), we quantify the bulk flow heterogeneity (on average, in the steady state) via the parameter δ_{het} , plotted as a function of the imposed stress for several different levels of wall roughness. For imposed stresses $\sigma < \sigma_Y$, both $\sqrt{\Lambda}$ and $\dot{\gamma}_{\text{bulk}}$ which appear in the definition of δ_{het} , are very small and do not attain a steady state, as indicated by the open symbols (therefore, the large error bar). We have, however, observed that the value of the flow heterogeneity itself is stationary during creep, which enables the calculation of a meaningful average. The results clearly indicate an increase of the heterogeneity with decreasing imposed stress as $\delta_{\text{het}} \sim \sigma^{-0.8}$. It is relatively independent of

wall roughness, showing that the effects of the wall persist only a few particle diameters into the bulk. This result suggests that the dynamical heterogeneity diverges at $\sigma \rightarrow 0$ under conditions of imposed stress, distinct from the divergent avalanche size seen at low imposed strain rate $\dot{\gamma} \rightarrow 0$ [54].

C. Transient dynamics and creep curves

We now investigate the transient evolution as a function of the time t since the imposition of a constant stress σ on a sample that is freshly prepared then aged for a waiting time $t_w = 50.0$, before shearing starts at $t = 0$. In particular, we explore the dynamical yielding process via which a regime of initial creep, with a strain rate that decreases over time, gives way to a final steady-state flow.

Figures 8(a) and 8(b) show the apparent shear rate (as measured via the relative wall speeds and so including the effects of slip) as a function of time t for a rough wall (a) and smooth wall (b). In each case, data are shown for five imposed stress values in separate curve bundles. The highest three stress values are all above the yield stress, $\sigma > \sigma_Y = 0.055$. Here, the apparent shear rate $\dot{\gamma}_{\text{wall}}$ initially decreases as a function of time, before attaining a minimum. The sample then yields, and the shear rate increases to attain a steady-flowing state. For the two lowest stress values, for which $\sigma < \sigma_Y$, the apparent shear rate attains a steady state only for smooth walls. This is due to the confounding effects of slip: with rough walls, where slip is suppressed and $\dot{\gamma}_{\text{wall}}$ coincides with the true bulk shear rate $\dot{\gamma}_{\text{bulk}}$, the shear rate never attains a steady state but continues to slowly decrease.

For the same five values of stress, the true bulk shear rate is shown as a function of time in Fig. 8(c). The curve bundle for each stress value now shows results for the six values of wall roughness explored in the flow curves of Fig. 5. Now that

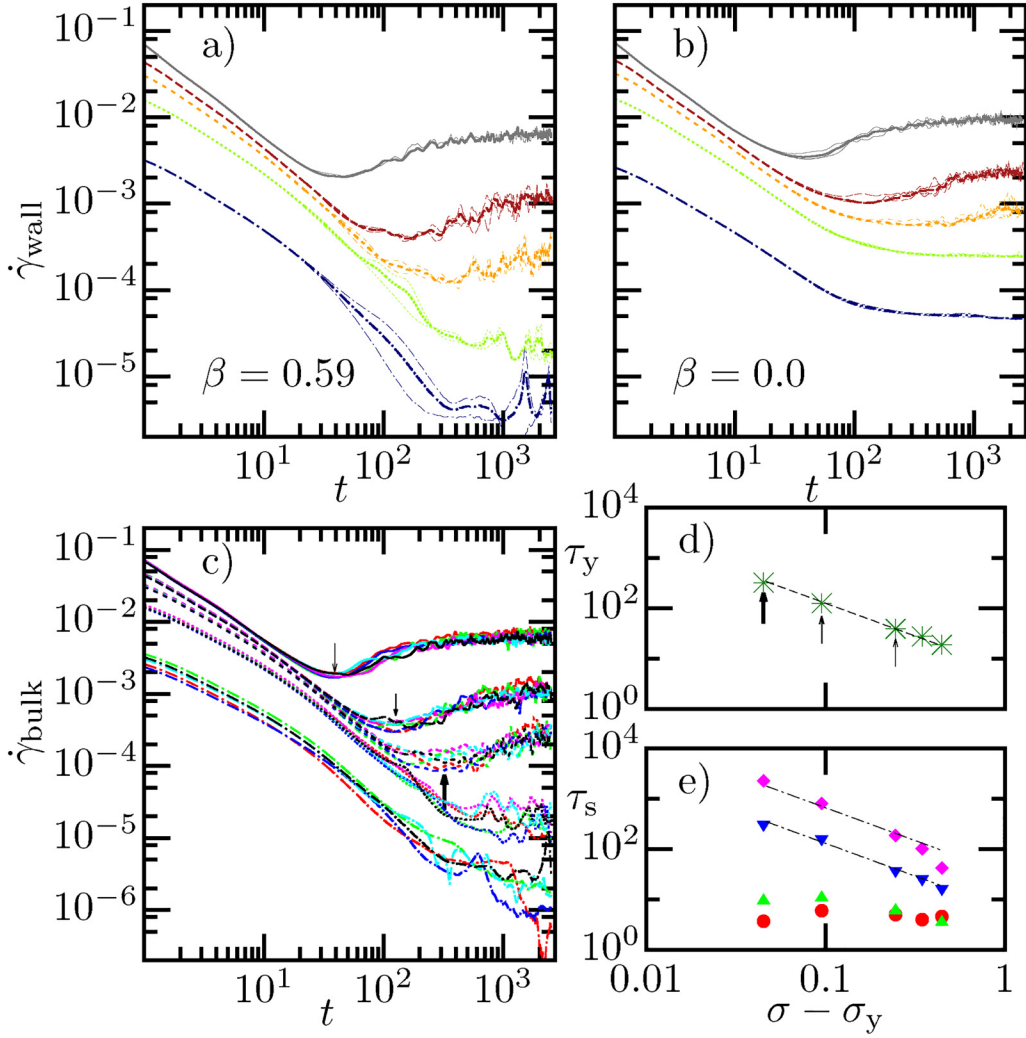


FIG. 8. Apparent shear rate vs time for shear stresses $\sigma = 0.3, 0.15, 0.1, 0.05, 0.01$ in curve bundles downwards for (a) a rough wall and (b) a smooth wall. (In each bundle, the thick line shows the average over 2 or 4 runs; thin lines show individual runs.) (c) Corresponding true shear rate vs time for the same imposed stresses. (In each bundle, curves are for several roughnesses, with color code as in Fig. 5. For each roughness, the curve is averaged over 2 or 4 runs.) (d) Yielding time τ_y at the minimum in $\dot{\gamma}_{\text{bulk}}(t)$ (averaged over roughnesses), as a function of stress above yield. Dotted line: power -1.3 . [Arrows denoting times in (c) and (d) coincide.] (e) Time τ_s at which wall slip velocity V_s attains half its steady-state value for the four smoothest walls, with roughness symbols as in Fig. 5. Dotted-dashed line: power -1.3 .

the effects of wall slip have been removed by plotting $\dot{\gamma}_{\text{bulk}}(t)$, the data for all wall roughnesses essentially coincide. In this way, we find the yielding dynamics in the fluid bulk to be largely independent of wall roughness. We extract by eye the time at the minimum in $\dot{\gamma}_{\text{bulk}}$ and define this to be the time τ_y at which yielding occurs. This shows a good fit to $\tau \sim (\sigma - \sigma_y)^{-1.3}$ [Fig. 8(d)]. Similarly, we determine the time τ_s at which slip first arises at the wall (defined as the time at which $V_s(t)$ attains half its steady-state value). We plot this as a function of $\sigma - \sigma_y$ in Fig. 8(e) for the four lowest values of wall roughness explored in the flow curves of Fig. 5. (For the two roughest walls in Fig. 5, no appreciable slip arises.) This slip timescale increases with increasing wall roughness. For the largest two roughness values at which slip occurs, τ_s further appears to depend on stress in the same way as the timescale for bulk yielding, with $\tau_s \sim (\sigma - \sigma_y)^{-1.3}$. Whether slip pre-empts bulk yielding (or vice versa), as determined by the prefactor, however, depends on the roughness.

V. CONCLUSIONS

To summarize, we have introduced a method for simulating the dynamics of a dense athermal suspension of soft particles sheared between hard walls of any roughness profile in order to study the key rheological phenomenon of wall slip. For imposed stresses below the bulk yield stress, we have shown the wall slip to be dominated by a thin solvent layer adjacent to the wall. In contrast, for imposed stresses above yield, we find an additional slip contribution arising from the fluidization of the first few particle layers. We have further characterized the scaling of slip velocity with imposed stress and demonstrated a transition from strong to suppressed slip with increasing wall roughness. We have also characterized the dependence of the timescale for yielding within the bulk fluid on the imposed stress and of the timescale for slipping at the wall as a function of both imposed stress and wall roughness. In future, it would be interesting to study slip in less concentrated soft suspensions, below jamming; rougher wall profiles to address a return

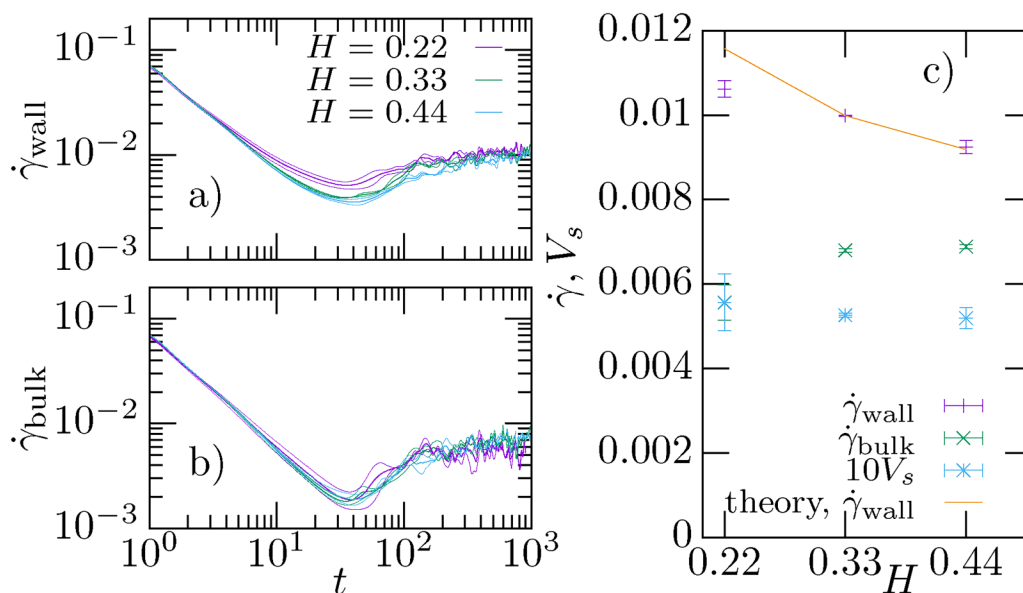


FIG. 9. Dependence on wall separation H of (a) the wall shear rate $\dot{\gamma}_{\text{wall}}$, (b) the true shear rate $\dot{\gamma}_{\text{bulk}}$, and (c) steady-state values of the former two quantities and the slip velocity V_s . The orange “theory” curve is defined as $\dot{\gamma}_{\text{wall}}(H) = 2V_s(H = 0.44)/H + \dot{\gamma}_{\text{bulk}}(H = 0.44)$. Definitions of $\dot{\gamma}_{\text{wall}}$, $\dot{\gamma}_{\text{bulk}}$, and V_s are given in the main text.

of slip for roughnesses exceeding the particle diameter [26]; and different interaction potentials with the wall.

Since this paper was written, we have become aware of a paper studying the effects of wall slip on a dense suspension of droplets in steady-state pressure driven flow along a channel [55]. It focuses entirely on steady-state behavior, presenting results for the mass throughput along the channel as a function of wall shear stress and wall roughness.

ACKNOWLEDGMENTS

The authors thank Thibaut Divoux for discussions. This work was funded by the Deutsche Forschungsgemeinschaft (DFG, German Research Foundation)—Project No. 233630050—TRR 146.

APPENDIX: FINITE SIZE EFFECTS

Since collective plastic rearrangements as well as long-range hydrodynamics can lead to many-body interactions that span several particle diameters, one can expect substantial finite size effects if the wall separation of the channel is too small. In Fig. 9, we show results for the transient evolution of the strain rate as a function of the time t since the imposition of a constant stress σ for different wall separations H . The apparent shear rate $\dot{\gamma}_{\text{wall}}$ indeed shows significant finite size effects (see panel a). This result is anticipated because it consists of two contributions,

$$\dot{\gamma}_{\text{wall}}(H) = 2V_s/H + \dot{\gamma}_{\text{bulk}}, \quad (\text{A1})$$

including the true shear rate in the bulk $\dot{\gamma}_{\text{bulk}}$ (see panel b) and the slip velocity, V_s , both of which are assumed to not depend on the wall separation. The latter assumption is investigated by comparing the steady-state values of the three

quantities (see panel c), and indeed no significant deviation can be found for $H > 0.3$ (it seems that the bulk flow for $H = 0.22$ is slightly slower than calculated for large channels). Using Eq. (A1), we can show that the dependence of $\dot{\gamma}_{\text{wall}}$ on wall separation can actually be explained with the trivial dependence on the (inverse) wall separation. Inverting this argument highlights a straightforward method to determine the slip velocity. Indeed, this is how slip was measured before the development of advanced experimental techniques like flow velocimetry [18].

REFERENCES

- [1] Seth, J. R., L. Mohan, C. Locatelli-Champagne, M. Cloitre, and R. T. Bonnecaze, “A micromechanical model to predict the flow of soft particle glasses,” *Nat. Mater.* **10**, 838–843 (2011).
- [2] Cohen-Addad, S., and R. Höhler, “Rheology of foams and highly concentrated emulsions,” *Curr. Opin. Colloid Interface Sci.* **19**, 536–548 (2014).
- [3] Fujii, S., and W. Richtering, “Size and viscoelasticity of spatially confined multilamellar vesicles,” *Eur. Phys. J. E* **19**, 139–148 (2006).
- [4] Cloitre, M., and D. Vlassopoulos, Block copolymers in external fields: Rheology, flow-induced phenomena, and applications, in *Applied Polymer Rheology: Polymeric Fluids with Industrial Applications* (Wiley, New York, 2011), pp. 209–239.
- [5] Vlassopoulos, D., and G. Fytas, “From polymers to colloids: Engineering the dynamic properties of hairy particles,” in *High Solid Dispersions* (Springer, Berlin, 2009), pp. 1–54.
- [6] Divoux, T., C. Barentin, and S. Manneville, “From stress-induced fluidization processes to Herschel-Bulkley behaviour in simple yield stress fluids,” *Soft Matter* **7**, 8409–8418 (2011).
- [7] Bonn, D., M. M. Denn, L. Berthier, T. Divoux, and S. Manneville, “Yield stress materials in soft condensed matter,” *Rev. Mod. Phys.* **89**, 035005 (2017).
- [8] Divoux, T., D. Tamarii, C. Barentin, S. Teitel, and S. Manneville, “Yielding dynamics of a Herschel–Bulkley fluid: A critical-like fluidization behaviour,” *Soft Matter* **8**, 4151–4164 (2012).

- [9] Cloitre, M., and R. T. Bonnecaze, "A review on wall slip in high solid dispersions," *Rheol. Acta* **56**, 283–305 (2017).
- [10] Barnes, H. A., "A review of the slip (wall depletion) of polymer solutions, emulsions and particle suspensions in viscometers: Its cause, character, and cure," *J. Nonnewton. Fluid Mech.* **56**, 221–251 (1995).
- [11] Vinogradov, G., G. Froishteter, K. Trilisky, and E. Smorodinsky, "The flow of plastic disperse systems in the presence of the wall effect," *Rheol. Acta* **14**, 765–775 (1975).
- [12] Vinogradov, G., G. Froishteter, and K. Trilisky, "The generalized theory of flow of plastic disperse systems with account of the wall effect," *Rheol. Acta* **17**, 156–165 (1978).
- [13] Dimitriou, C. J., and G. H. McKinley, "A comprehensive constitutive law for waxy crude oil: A thixotropic yield stress fluid," *Soft Matter* **10**, 6619–6644 (2014).
- [14] Meeker, S. P., R. T. Bonnecaze, and M. Cloitre, "Slip and flow in pastes of soft particles: Direct observation and rheology," *J. Rheol.* **48**, 1295–1320 (2004).
- [15] Joseph, D. D., R. Bai, K. Chen, and Y. Y. Renardy, "Core-annular flows," *Annu. Rev. Fluid Mech.* **29**, 65–90 (1997).
- [16] Stokes, J. R., M. W. Boehm, and S. K. Baier, "Oral processing, texture and mouthfeel: From rheology to tribology and beyond," *Curr. Opin. Colloid Interface Sci.* **18**, 349–359 (2013).
- [17] Roman, S., A. Merlo, P. Duru, F. Risso, and S. Lorthois, "Going beyond 20 μm -sized channels for studying red blood cell phase separation in microfluidic bifurcations," *Biomicrofluidics* **10**, 034103 (2016).
- [18] Yoshimura, A., and R. K. Prud'homme, "Wall slip corrections for couette and parallel disk viscometers," *J. Rheol.* **32**, 53–67 (1988).
- [19] Meeker, S. P., R. T. Bonnecaze, and M. Cloitre, "Slip and flow in soft particle pastes," *Phys. Rev. Lett.* **92**, 198302 (2004).
- [20] Poumaere, A., M. Moyers-González, C. Castelain, and T. Burghellea, "Unsteady laminar flows of a carbopol® gel in the presence of wall slip," *J. Nonnewton. Fluid Mech.* **205**, 28–40 (2014).
- [21] Salmon, J.-B., L. Bécu, S. Manneville, and A. Colin, "Towards local rheology of emulsions under couette flow using dynamic light scattering," *Eur. Phys. J. E* **10**, 209–221 (2003).
- [22] Geraud, B., L. Bocquet, and C. Barentin, "Confined flows of a polymer microgel," *Eur. Phys. J. E* **36**, 30 (2013).
- [23] Péméja, J., B. Géraud, C. Barentin, and M. Le Merrer, "Wall slip regimes in jammed suspensions of soft microgels," *Phys. Rev. Fluids* **4**, 033301 (2019).
- [24] Seth, J. R., C. Locatelli-Champagne, F. Monti, R. T. Bonnecaze, and M. Cloitre, "How do soft particle glasses yield and flow near solid surfaces?," *Soft Matter* **8**, 140–148 (2012).
- [25] Pérez-González, J., J. López-Durán, B. Marín-Santibáñez, and F. Rodríguez-González, "Rheo-PIV of a yield-stress fluid in a capillary with slip at the wall," *Rheol. Acta* **51**, 937–946 (2012).
- [26] Mansard, V., L. Bocquet, and A. Colin, "Boundary conditions for soft glassy flows: Slippage and surface fluidization," *Soft Matter* **10**, 6984–6989 (2014).
- [27] Zhang, X., E. Lorenceau, P. Basset, T. Bourouina, F. Rouyer, J. Goyon, and P. Coussot, "Wall slip of soft-jammed systems: A generic simple shear process," *Phys. Rev. Lett.* **119**, 208004 (2017).
- [28] Zhang, X., E. Lorenceau, T. Bourouina, P. Basset, T. Oerther, M. Ferrari, F. Rouyer, J. Goyon, and P. Coussot, "Wall slip mechanisms in direct and inverse emulsions," *J. Rheol.* **62**, 1495–1513 (2018).
- [29] Divoux, T., V. Lapeyre, V. Ravaine, and S. Manneville, "Wall slip across the jamming transition of soft thermoresponsive particles," *Phys. Rev. E* **92**, 060301(R) (2015).
- [30] Divoux, T., D. Tamarii, C. Barentin, and S. Manneville, "Transient shear banding in a simple yield stress fluid," *Phys. Rev. Lett.* **104**, 208301 (2010).
- [31] Grenard, V., T. Divoux, N. Taberlet, and S. Manneville, "Timescales in creep and yielding of attractive gels," *Soft Matter* **10**, 1555–1571 (2014).
- [32] Gibaud, T., C. Barentin, N. Taberlet, and S. Manneville, "Shear-induced fragmentation of laponite suspensions," *Soft Matter* **5**, 3026–3037 (2009).
- [33] Gibaud, T., D. Frelat, and S. Manneville, "Heterogeneous yielding dynamics in a colloidal gel," *Soft Matter* **6**, 3482–3488 (2010).
- [34] Gibaud, T., C. Barentin, and S. Manneville, "Influence of boundary conditions on yielding in a soft glassy material," *Phys. Rev. Lett.* **101**, 258302 (2008).
- [35] Kurokawa, A., V. Vidal, K. Kurita, T. Divoux, and S. Manneville, "Avalanche-like fluidization of a non-Brownian particle gel," *Soft Matter* **11**, 9026–9037 (2015).
- [36] Perge, C., N. Taberlet, T. Gibaud, and S. Manneville, "Time dependence in large amplitude oscillatory shear: A rheo-ultrasonic study of fatigue dynamics in a colloidal gel," *J. Rheol.* **58**, 1331–1357 (2014).
- [37] Goyon, J., A. Colin, G. Ovarlez, A. Ajdari, and L. Bocquet, "Spatial cooperativity in soft glassy flows," *Nature* **454**, 84–87 (2008).
- [38] Davies, G., and J. Stokes, "Thin film and high shear rheology of multiphase complex fluids," *J. Nonnewton. Fluid Mech.* **148**, 73–87 (2008).
- [39] Nicolas, A., and J.-L. Barrat, "A mesoscopic model for the rheology of soft amorphous solids, with application to microchannel flows," *Faraday Discuss.* **167**, 567–600 (2013).
- [40] Seth, J. R., M. Cloitre, and R. T. Bonnecaze, "Influence of short-range forces on wall-slip in microgel pastes," *J. Rheol.* **52**, 1241–1268 (2008).
- [41] Christel, M., R. Yahya, M. Albert, and B. A. Antoine, "Stick-slip control of the carbopol microgels on polymethyl methacrylate transparent smooth walls," *Soft Matter* **8**, 7365–7367 (2012).
- [42] Chan, H. K., and A. Mohraz, "A simple shear cell for the direct visualization of step-stress deformation in soft materials," *Rheol. Acta* **52**, 383–394 (2013).
- [43] Rahimian, A., S. K. Veerapaneni, and G. Biros, "Dynamic simulation of locally inextensible vesicles suspended in an arbitrary two-dimensional domain, a boundary integral method," *J. Comput. Phys.* **229**, 6466–6484 (2010).
- [44] Derzsi, L., D. Filippi, G. Mistura, M. Pierno, M. Lulli, M. Sbragaglia, M. Bernaschi, and P. Garstecki, "Fluidization and wall slip of soft glassy materials by controlled surface roughness," *Phys. Rev. E* **95**, 052602 (2017).
- [45] Derzsi, L., D. Filippi, M. Lulli, G. Mistura, M. Bernaschi, P. Garstecki, M. Sbragaglia, and M. Pierno, "Wall fluidization in two acts: From stiff to soft roughness," *Soft Matter* **14**, 1088–1093 (2018).
- [46] Plimpton, S., "Fast parallel algorithms for short-range molecular dynamics," *J. Comput. Phys.* **117**, 1–19 (1995).
- [47] Swope, W. C., H. C. Andersen, P. H. Berens, and K. R. Wilson, "A computer simulation method for the calculation of equilibrium constants for the formation of physical clusters of molecules: Application to small water clusters," *J. Chem. Phys.* **76**, 637–649 (1982).
- [48] Peskin, C. S., "The immersed boundary method," *Acta Numerica* **11**, 479–517 (2002).
- [49] Bao, Y., A. Donev, B. E. Griffith, D. M. McQueen, and C. S. Peskin, "An immersed boundary method with divergence-free velocity interpolation and force spreading," *J. Comput. Phys.* **347**, 183–206 (2017).
- [50] Yang, X., X. Zhang, Z. Li, and G.-W. He, "A smoothing technique for discrete delta functions with application to immersed boundary method in moving boundary simulations," *J. Comput. Phys.* **228**, 7821–7836 (2009).
- [51] Newren, P., Enhancing the immersed boundary method: Stability, volume conservation and implicit solvers, Ph.D. thesis, University of Utah, 2007.
- [52] Hemingway, E., A. Clarke, J. Pearson, and S. Fielding, "Thickening of viscoelastic flow in a model porous medium," *J. Nonnewton. Fluid Mech.* **251**, 56–68 (2018).

- [53] Derzsi, L., D. Filippi, G. Mistura, M. Pierno, M. Lulli, M. Sbragaglia, M. Bernaschi, and P. Garstecki, "Fluidization and wall slip of soft glassy materials by controlled surface roughness," *Phys. Rev. E* **95**, 052602 (2017).
- [54] Lemaître, A., and C. Caroli, "Rate-dependent avalanche size in athermally sheared amorphous solids," *Phys. Rev. Lett.* **103**, 065501 (2009).
- [55] Pelusi, F., M. Sbragaglia, A. Scagliarini, M. Lulli, M. Bernaschi, and S. Succi, "On the impact of controlled wall roughness shape on the flow of a soft material," *Europhys. Lett.* **127**, 34005 (2019).
- [56] See the supplementary material at <https://doi.org/10.1122/8.0000171> for movies of the yielding dynamics in two sample packings with flat and rough walls.